Title page

Severe Bending of Two Aortic Stent-Grafts: an Experimental and Numerical Mechanical Analysis

Nicolas Demanget[1,2], Pierre Latil[2], Laurent Orgéas[2], Pierre Badel[1], Stéphane Avril[1], Christian Geindreau[2], Jean-Noël Albertini[3], Jean-Pierre Favre[3]

[1] *Ecole Nationale Supérieure des Mines*
CIS-EMSE, CNRS UMR 5146
158 cours Fauriel
Saint-Etienne F-42023, France.

[2] *CNRS / Université de Grenoble (Grenoble-INP / UJF)*
Laboratoire Sols-Solides-Structures-Risques (3SR Lab)
BP 53, 38 041 Grenoble cedex 9, France.

[3] *CHU Hôpital Nord*
Department of Vascular Surgery
Saint-Etienne F-42055, France.

Abbreviated title: Severe Bending of Aortic Stent-Grafts

Correspondence:

Nicolas Demanget
158 cours Fauriel
Saint-Etienne F-42023, France.
+33 0 477499772
nicolas.demanget@gmail.com

Abstract and key terms

Stent grafts (SGs) are commonly used for treating abdominal aortic aneurysms (AAAs) and numerical models tend to be developed for predicting the biomechanical behavior of these devices. However, due to the complexity of SGs, it is important to validate the models. In this work, a validation of the numerical model developed in Demanget *et al*. (*J. Mech. Behav. Biomed. Mater*. 5:272-282, 2012) is presented. Two commercially available SGs were subjected to severe bending tests and their 3D geometries in undeformed and bent configurations were imaged from X-ray microtomography. Dedicated image processing subroutines were used in order to extract the stent centerlines from the 3D images. These skeletons in the undeformed configurations were used to set up SG numerical models that are subjected to the boundary conditions measured experimentally. Skeletons of imaged and deformed stents were then quantitatively compared to the numerical simulations. A good agreement is found between experiments and simulations. This validation offers promising perspectives to implementing the numerical models in a computer-aided tool and simulating the endovascular treatments.

Key terms: Endograft, Finite Element Analysis, X-Ray Microtomography

Introduction

A widely used and minimally invasive technique to prevent abdominal aortic aneurysm (AAA) rupture, endovascular aneurysm repair (EVAR), involves the endovascular insertion of a stent-graft (SG) via the femoral arteries in order to exclude the aneurysm sac from the main blood flow. Most recent SGs consist of a combination of Nitinol stents stitched onto a polymeric woven fabric. EVAR is associated with lower post-operative morbidity and mortality compared with the invasive traditional surgical procedure to treat AAA. However, SG durability remains a significant issue. During the patient's follow-up, complications requiring secondary interventions may occur, such as endoleaks [1, 5], stent fracture [17], wear of the polymeric woven fabric [6, 9] as well as stenosis or thrombosis of the SG [8, 10]. Insufficient flexibility of the devices was often considered as one of the main causes responsible for these complications, especially when the SGs are deployed in tortuous AAAs. This evidence clearly emphasizes the critical need to better understand and model the mechanical behavior of SGs.

In that sense, finite element (FE) analyses can be suitable to better study the deformation mechanisms responsible for the above-mentioned SG-related complications, to compare the clinical and mechanical performances of manufactured SGs and/or to guide choices during the SG design process. Though a fair amount of work was devoted to the FE modeling of the mechanics of stents alone [3, 15, 28], very few numerical studies have been conducted on the assessment of SGs mechanics [13, 19, 32]. This is partially due (i) to the complexity of SGs which combine stents stitched onto thin anisotropic and deformable membranes and (ii) to the difficulty to properly obtain the initial geometry of the SGs:

(i) With the help of some simplifying assumptions (in particular for the stitching model), the first point can be overcome [13, 19, 32]. For example, numerical models (including

both stents and grafts) of manufactured SGs were developed to analyze the influence of the stent architecture on the bending behavior of SGs [13]. However, no study was carried out to validate finely these SG numerical models and/or confront simulation results with experimental data.

(ii) A possible solution to prevent from the second difficulty consists in obtaining the initial geometries of SGs directly from 3D images, *e.g.* with X-ray microtomography. This imaging technique is an attractive tool for experimental mechanics [7, 29, 30]. Within the field of medical devices, it was purposely used in order to image the *in-vitro* deployment steps of coronary stents [11] or to model their initial geometry after suitable image analysis subroutines [24]. Furthermore, an automatic method has been recently developed to segment the stents of SGs from CT data [18]. Besides, it is important to notice that if a proper mechanical testing device could be inserted inside a microtomograph, X-ray microtomography could also be used to catch SGs geometries when the SGs are subjected to a mechanical loading, as already carried out for other fibrous structures and architectures [4, 20, 21]. These *in situ* 3D observations could thus provide useful data in order to check the validity of SG numerical models.

Within this context, the aim of the present study is to validate the numerical technique developed by Demanget *et al.* [13] in order to predict the deformation of SGs. To do so, the methodology sketched in figure 1 was followed. Two commercially available SGs were subjected to bending tests and their geometries in the undeformed and bent configurations were scanned with an X-ray microtomograph. The image analysis subroutines developed in Latil *et al.* (2011) [20] were then used in order to extract descriptors of the stent centerlines from the 3D images. The skeletons of the initial stent were also used to process relevant numerical models of the SGs that were subjected to the boundary conditions very close to those

measured experimentally. The skeletons of the deformed and imaged stents were finally used to validate the numerical simulations.

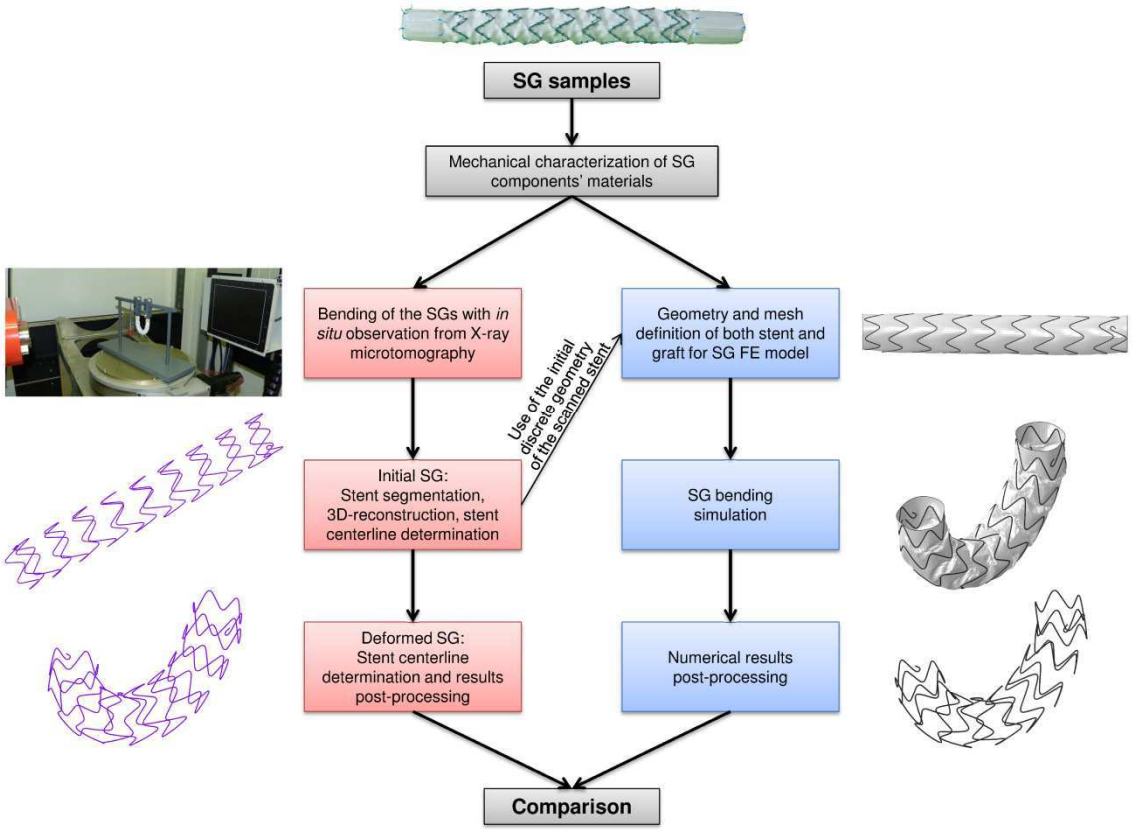

Figure 1 - Scheme of the study outline.

Materials and methods

a. Stent-grafts

Common tortuosity of iliac arteries and its related postoperative complications, *e.g.* SG thrombosis or stenosis, guided our choice to the study of SG iliac limbs. Indeed, these devices are usually subjected to important deformations during and after their deployment within iliac arteries. Limb samples were thus obtained from manufacturers. Two SG limbs of last generation, *i.e.* Aorfix (Ao-SG, Lombard Medical, Didcot, United Kingdom) and Zenith Spiral-Z (Zs-SG, Cook Medical Europe, Bjaeverskov, Denmark), were considered in the present work. They are displayed in figure 2.

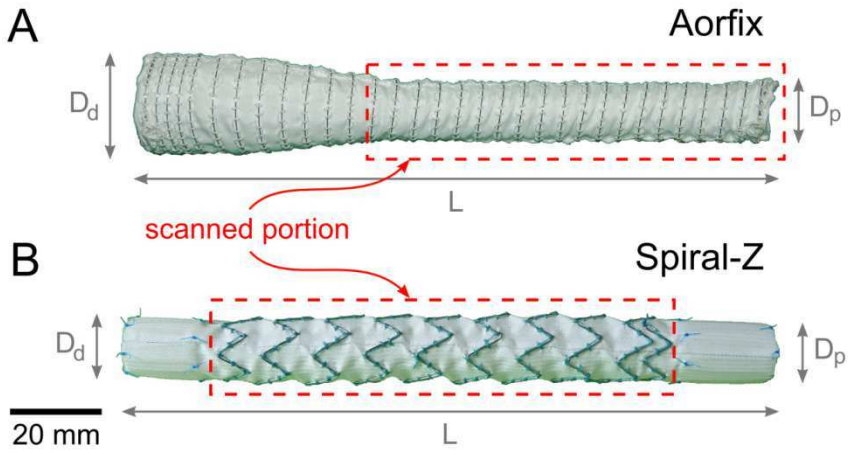

Figure 2 - Pictures of the two considered SG limbs.

Ao-SG was first implanted in human in 2001. Its iliac limb is composed of a continuous external spiral NiTi (Nitinol Shape Memory Alloy) stent stitched onto a polyester woven fabric (Dacron) with polyester running sutures. The main dimensions of the limbs were as follows: proximal D_p and distal D_d diameters of 12 and 16 mm, respectively; total length L of 110 mm.

The first human implantation of Zs-SG was performed in 2008. This device is composed of a continuous external spiral-Z combination NiTi stent stitched onto a polyester woven fabric (Dacron) with polyester running sutures. Dimensions of the sample were as follows: both proximal D_p and distal D_d diameters of 13 mm; total length L of 144 mm. Proximal and distal Z-stents were independent and internal to the fabric and their length was 21 and 17 mm, respectively.

b. 3D *in situ* observations of SGs bending

As sketched in figure 1, the aim of this experimental analysis was (i) to provide initial (undeformed) geometries of the two considered stents and (ii) to assess some quantitative comparison criteria from 3D images of the deformed stents. The whole process to perform experimental SG bending and to post-process tomographic data is reported hereafter.

i. X-ray microtomography set-up

3D images of the undeformed and deformed SGs were obtained using a laboratory X-ray microtomograph (3SR Lab, Grenoble, France, RX Solutions apparatus). As illustrated in figure 3, it consists of a microfocus enclosed tube (1) (conical X-ray source, voltage from 40 to 150 kV, current intensity up to 500 µA) and a large detector (2) (195.07×243 mm^2 with a field of view of 1920×1536 pixels^2). For the present experiments, the generator voltage and current were respectively set to 100 kV and 290 µA. The acquisition rate was set to 10 images/s and 900 images were acquired on a 360° rotation (3) of the scanned SG. Besides, the 3D images of the sample were obtained from the 900 radiographs by using commercial reconstruction software (using backprojections algorithm, DigiCT, Digisens, France). Finally, a voxel size of 57 x 57 x 57 µm^3 was chosen in order to have the full structure of the SG together with rather good spatial definition of stent cross sections. If these settings could not

provide a good representation of the polymer graft, it provides in return a very nice imaging of the stents together with short scanning times.

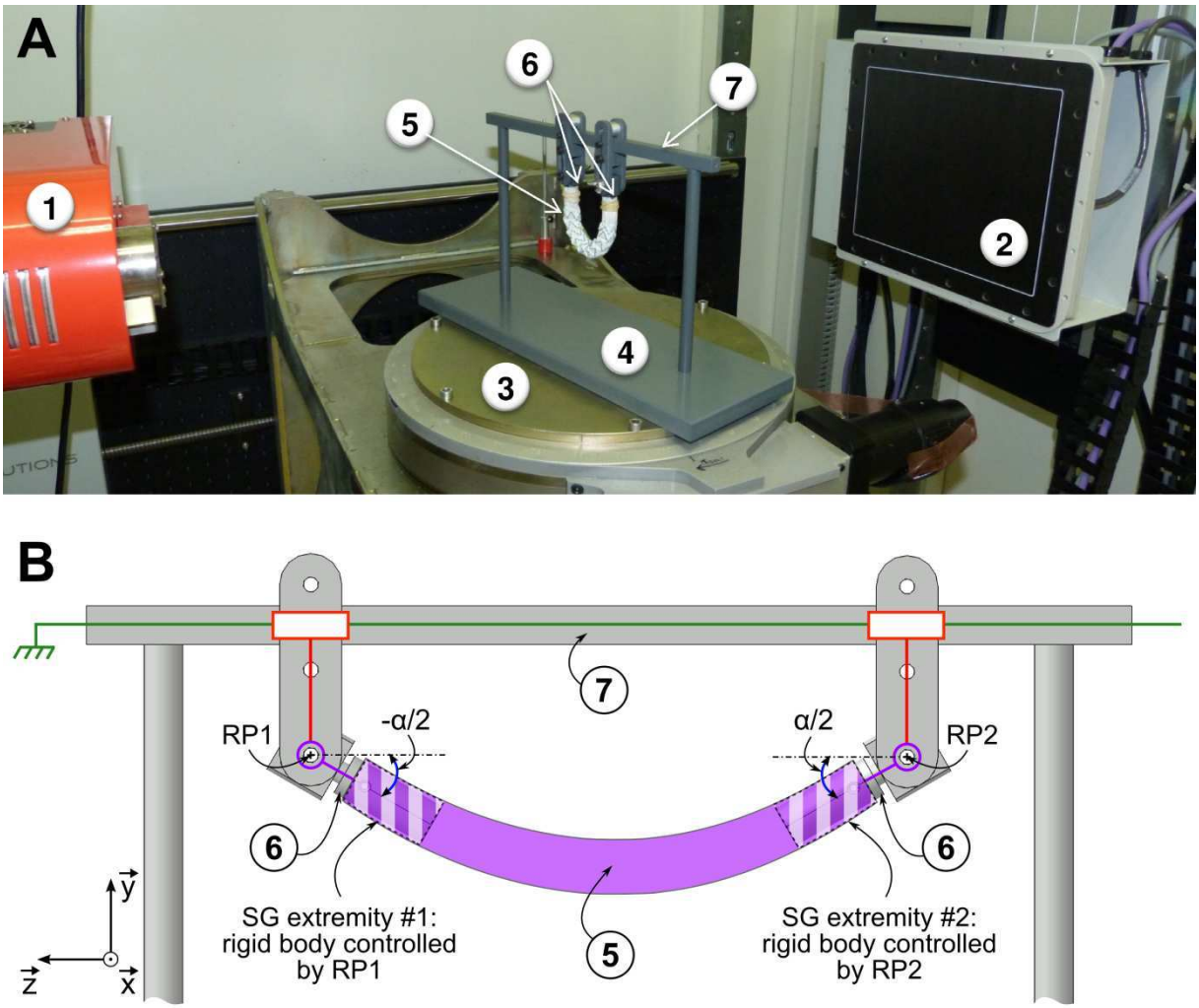

Figure 3 - Picture and scheme of the *in situ* bending device mounted in the X-ray microtomograph (3SR Lab). (1) X-ray source, (2) Detector, (3) Rotary stage, (4) Bending device, (5) Stent-graft (SG), (6) Brackets, (7) Longitudinal support bar.

ii. Detection of stent centerlines

After proper denoising operations (standard smoothing and filtering algorithms), the 3D images could be segmented (with the software ImageJ) in order to have 3D representations of

the stents (see figure 1). SG centerlines were then obtained by using the skeletonization algorithms implemented in the commercial software Avizo (VSG). The centerlines then consisted of a list of points whose spatial coordinates were expressed in the 3D image reference frame. As shown in figure 4, the noisy poly-lines defined from these points were finally smoothed using a homemade Matlab routine based on a moving average.

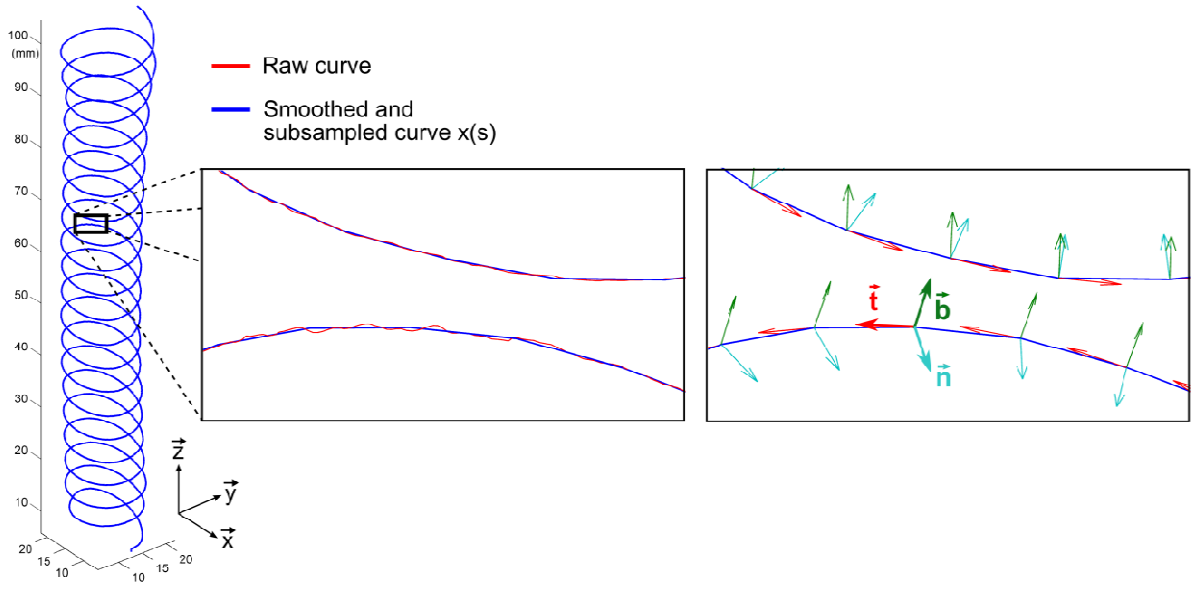

Figure 4 - 3D representation of the raw and smoothed data obtained from the Ao-SG centerline extraction (two left graphs). Definition of the local Frenet bases (right graph).

iii. Bending device

An experimental bending device was designed, manufactured and used to perform bending tests on the considered SG limbs. It is illustrated in figure 3. Most of its components were made up of polyvinyl chloride (PVC) in order not to disturb the X-ray beam during the SGs scans. The SG limbs ends were embedded on the brackets (6) and then mounted on the support bar (7) (see figure 3). For the Ao-SG limb, only the portion of the stent with a global diameter approximately equal to 12 mm was studied: the SG distal end was rolled up and fixed on a bracket. As a consequence, the length of the considered Ao stent which was

subjected to the bending was about 100 mm. Proximal and distal Z-stents of Zs-SG were fully embedded on the brackets so that both Z-spiral stent ends were also attached on the brackets. Only the central continuous Z-spiral stent was considered and studied in the present work: the length of the considered stent was about 100 mm.

The experimental device allowed to subject each SG end to opposite rotations about the *x*-axis, until a bending angle α of 180° was reached (see figure 3). The maximum value of 180° for α was based on clinical data provided by our surgical team [2]. In order to maintain the SG in the *yz*-plane, the other two rotations were locked. Only the translation of the SG ends along the *z*-axis, *i.e.* the longitudinal direction of the SG, was let free in order to avoid spurious tension in the fabric during SG bending. Once the deformed SG reached its equilibrium on the experimental bending device, the translation along *z*-axis was locked in order to have a stable experimental device during tomographic acquisitions.

c. Bending simulation

Both geometry and mechanical behavior of the two considered SG limbs were modeled using the finite element analysis software Abaqus 6.8/Explicit® (Simulia). The whole methodology to simulate SGs bending was similar to that carried out previously [13]. It is briefly recalled hereafter.

i. Material properties

Stents of both limbs were made up of NiTi whose the superelastic properties were taken from literature [19] and given in table 1. The tension/compression asymmetry often observed in NiTi alloys [25, 26] was neglected in this study for simplicity. In addition, it was assumed that stents' material points were subjected to a monotonic loading during the SGs bending, *i.e.* without unloading. As in Demanget *et al.* (2012) [13], this assumption was checked *a posteriori* and enabled us to use a simple and standard elasto-plastic constitutive model for the NiTi

stents. Doing so, as sketched in figure 5, the standard yield stress corresponded to the onset of the forward stress-induced martensitic transformation σ_L^S, below which the behavior corresponds to the elasticity of the austenite phase (Young's modulus E_A, Poisson's ratio ν_A). Above the yield stress, a bilinear strain hardening was chosen to describe both the forward stress-induced martensitic transformation (up to a transformation strain ε^L) and the elasticity of the martensite phase (Young's modulus E_M, Poisson's ratio ν_M).

Table 1 Material properties of Nitinol

Parameters	**Values**
Austenite elasticity E_A(MPa)	40000
Austenite Poisson's ratio ν_A	0.46
Martensite elasticity E_M (MPa)	18554
Martensite Poisson's ratio ν_M	0.46
Transformation strain ε^L	0.04
Start of transformation loading σ_L^S (MPa)	390
End of transformation loading σ_L^E (MPa)	425
Ultimate tensile strength σ_R (MPa)	827 – 1172

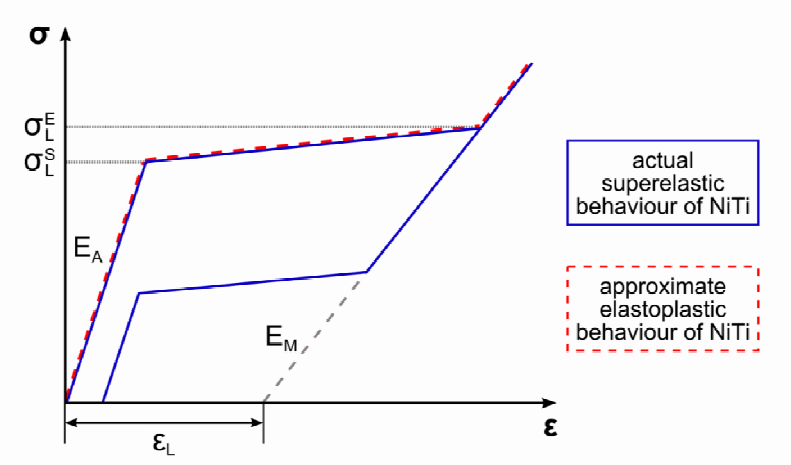

Figure 5 - Schematic stress-strain curve of a superelastic Nitinol.

The lack of data concerning the mechanical properties of the SGs polyester fabrics led us to perform our own mechanical tests with fabric samples obtained from manufacturers. As described in Demanget *et al.* (2012) [13], by assuming as a first approximation that the fabrics behaved as orthotropic elastic plates, this methodology combines:

- several pure and plane strain tensile tests, to determine the in-plane orthotropic elastic behavior of the fabrics with longitudinal E_L and transverse E_T Young's moduli, a Poisson's ratio ν_{LT} and a shear modulus G (see table 2),
- "nail tests", to estimate the longitudinal D_L and transverse D_T bending stiffnesses of the fabrics (see table 2).

Table 2 Material properties of both fabrics

Parameters	**Ao-fabric**	**Zs-fabric**
E_L (MPa)	260 ± 4%	225 ± 10%
E_T (MPa)	110 ± 12%	1000 ± 10%
ν_{LT}	0.2	0.2
G (MPa)	0.4	3.6
Longitudinal ultimate strain ε_R^L	0.40	0.23
Circumferential ultimate strain ε_R^C	0.13	0.18
Longitudinal bending stiffness D_L (10^{-4} Nmm)	4.6	4.0
Circumferential bending stiffness D_C (10^{-4} Nmm)	2.0	18

ii. Geometry and mesh

Stent geometries were meshed with beam elements (B31 in Abaqus) instead of volume elements in order to reduce the computational cost of simulations (see table 3). This simplification of stent modeling was used in several studies since Hall and Kasper (2006) [16] showed that this approximation yielded acceptable results when studying the global stent stress state.

Table 3 Geometrical and computational features of numerical SG models

	Ao-SG	**Zs-SG**
Degrees Of Freedom (DOF)	77676	75090
Graft		
Fabric thickness (mm)	0.10	0.08
Number of elements	26600	20336
Stents		
Wire radius *r* (mm)	0.125	0.17
Number of elements	2756	2282

As in Elliott *et al*. (2002), undeformed stent geometries were directly derived from the smoothed list of points generated through tomographic data post-processing (see figure 1). A homemade Matlab routine was created purposely to sample these coordinates and generate the nodes as well as the connectivity of the B31 elements of the stent.

Since the 3D-reconstruction of the textile from tomography was not available, it was necessary to create geometry and mesh of the graft which was fixed onto the stent. The

following procedure was chosen to perform this complex operation. A cylindrical tube meshed with linear triangular shell elements (S3 in Abaqus) was modeled and pressurized within the stent (considered as a rigid body at this stage) in order to fit stent geometry as close as possible (see figure 6). During the pressurization, translation about the *z*-axis was fixed at both graft ends. This first step of graft positioning was improved by changing temporally the fabric mechanical properties, *i.e.* E_L was increased while E_C was decreased in order to avoid graft bulging between stent turns. Once the graft was well positioned onto the stents, the stress field in the graft was set to zero. This configuration was defined as the undeformed configuration for the bending simulations.

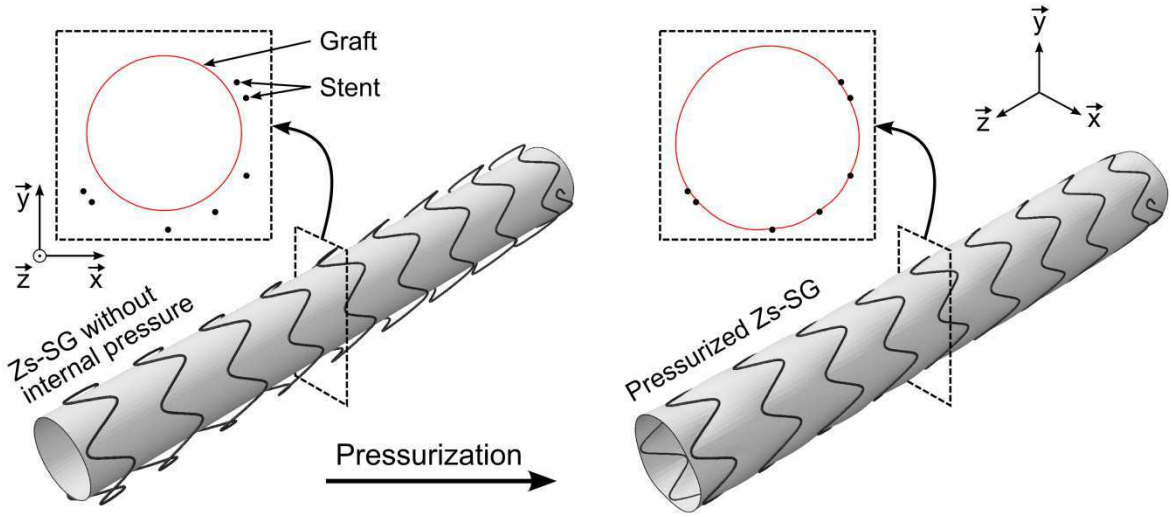

Figure 6 - Graft positioning step by SG pressurization: 3D views and associated cross-sections.

Likewise, sutures securing the stents and the graft together were modeled through the imposition of a bonding between graft and stent outer surfaces (tie constraint in Abaqus), *i.e.* no sliding was allowed between stent and graft. Lastly, a self-contact algorithm was added in order to avoid self-penetration of SG components.

iii. Boundary conditions

Numerical boundary conditions were applied on two reference points (RP1 and RP2) controlling both SG ends considered as rigid bodies. RP1 and RP2 were placed at the exact location of both pivot links, as depicted on figure 3. The SG portions mounted on brackets in the experimental device were considered as rigid bodies. Boundary conditions consisted in applying opposite rotations (until reaching α = 180°) about the *x*-axis at each RP while locking the two other rotations together with the *x* and *y*-axes translations. The displacement of SG ends along the *z*-axis was measured during experimental bending and then imposed numerically to adjust numerical boundary conditions to the nearest experimental measurements.

d. Quantitative comparison between experiments and simulations

This comparison was based on the analysis of the stents' centerline geometries in the deformed experimental and numerical configurations. As summarized in figure 1, these centerlines were obtained from 3D images as well as from simulation results. Thus, by noting *s* the curvilinear abscissa of the considered centerlines, the position *x(s)* of each centerline was characterized, together with its corresponding Frenet basis (**t**,**n**,**b**) [20], as shown in figure 4:

$$\mathbf{t} = \frac{\mathrm{d}\mathbf{x}}{\mathrm{d}s}, \quad \mathbf{n} = \frac{1}{\kappa}\frac{\mathrm{d}\mathbf{t}}{\mathrm{d}s}, \quad \mathbf{b} = \mathbf{t}\times\mathbf{n}, \tag{2}$$

where $\kappa(s)$ is the local curvature of the considered centerline. A similar procedure was also carried out for the undeformed configurations, where the local centerline curvature was noted $\kappa_0(s)$. Note that the chosen spatial resolution together with the skeletonization/smoothing procedure induced a small systematic error $\Delta\kappa \approx \pm 0.01$ mm^{-1} on the estimation of the curvatures. Thereafter, by noting that the experimental and numerical length of the considered stents remained constant after bending, *i.e.* that stents' centerlines were subjected to negligible tensile elongation, it was then possible to follow the material points of the centerlines from the undeformed to the deformed experimental and numerical configurations.

The comparison of the experimental and numerical curvature $\kappa(s)$ could then be achieved at each of these material points in the deformed configurations. Besides, the distance $\Delta x(s)$ between each associated couple of material points of the experimental ($x_{exp}(s)$) and the numerical ($x_{num}(s)$) deformed centerlines was also calculated ($\Delta x(s) = ||x_{exp}(s) - x_{num}(s)||$), and a 3D position error

$$\delta(s) = \Delta x(s) / R \tag{3}$$

was defined from the largest displacement along the stent, corresponding approximately to the global radius of curvature R of the bent stent (see figure 8). Lastly, from the knowledge of the stent wire radius r and the local curvatures in the initial $\kappa_0(s)$ and deformed $\kappa(s)$ configurations, it was also possible to estimate the local maximal bending strain $\varepsilon_b^{max}(s)$ the stents were subjected to during their deformation:

$$\varepsilon_b^{\max} = r\left|\kappa - \kappa_0\right| \tag{4}$$

Taking into account the error induced during the estimation of the curvatures, note that such maximal bending strain were estimated with a very small error $\Delta\varepsilon_b^{max} = 2.10^{-3}$.

Results

a. Qualitative comparison

Figure 7 gives a first qualitative comparison of deformed and simulated Zs-SG. A similar comparison could be carried out with Ao-SG. As shown from this figure, the global shapes of the experimental and simulated bent SGs are very close, bearing in mind the complexity of the numerical boundary values problems. In particular, this figure shows that the wrinkling modes of the woven polymer textile between the stents are similar to those observed experimentally, at least semi-quantitatively.

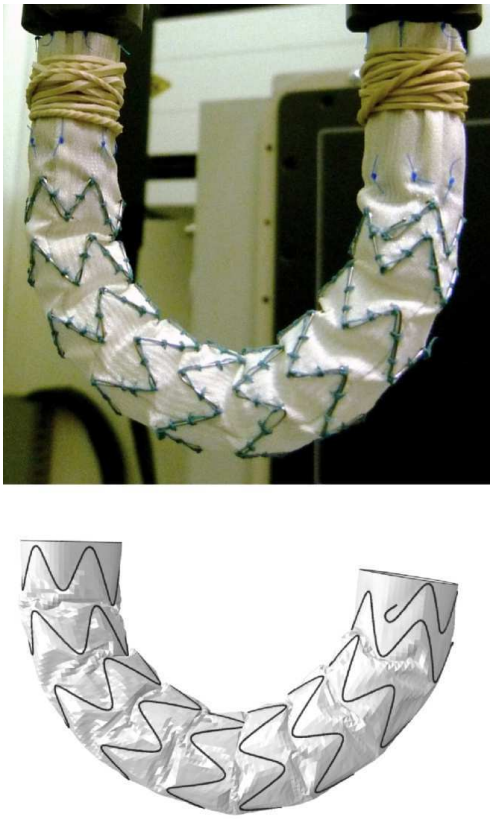

Figure 7 - Global shapes of actual (upper picture) and simulated (lower picture) bent Zs-SGs.

Figure 8 strengthens the above-mentioned remarks, by comparing the 3D experimental and simulated shapes of deformed stents' centerlines for both SGs. As obvious from this figure, the simulated centerlines are close from experimental ones. However, some differences can be noted. For example, as revealed from the front views displayed in figure 8, the overall bending of the SGs, *i.e.* the bending of the SGs' centerlines, is somewhat more pronounced for the experimental SGs than for the numerical ones. Besides, by looking more closely at the deformed shapes of the stents in the case of Ao-SG, a significant difference between experimental and numerical centerlines is observed and concerned the fifth turn from the SG end #1: the turn of experimental stent seems to get inside the SG and generated a localized stent deformation while the global shape of numerical stent remained fairly homogeneous.

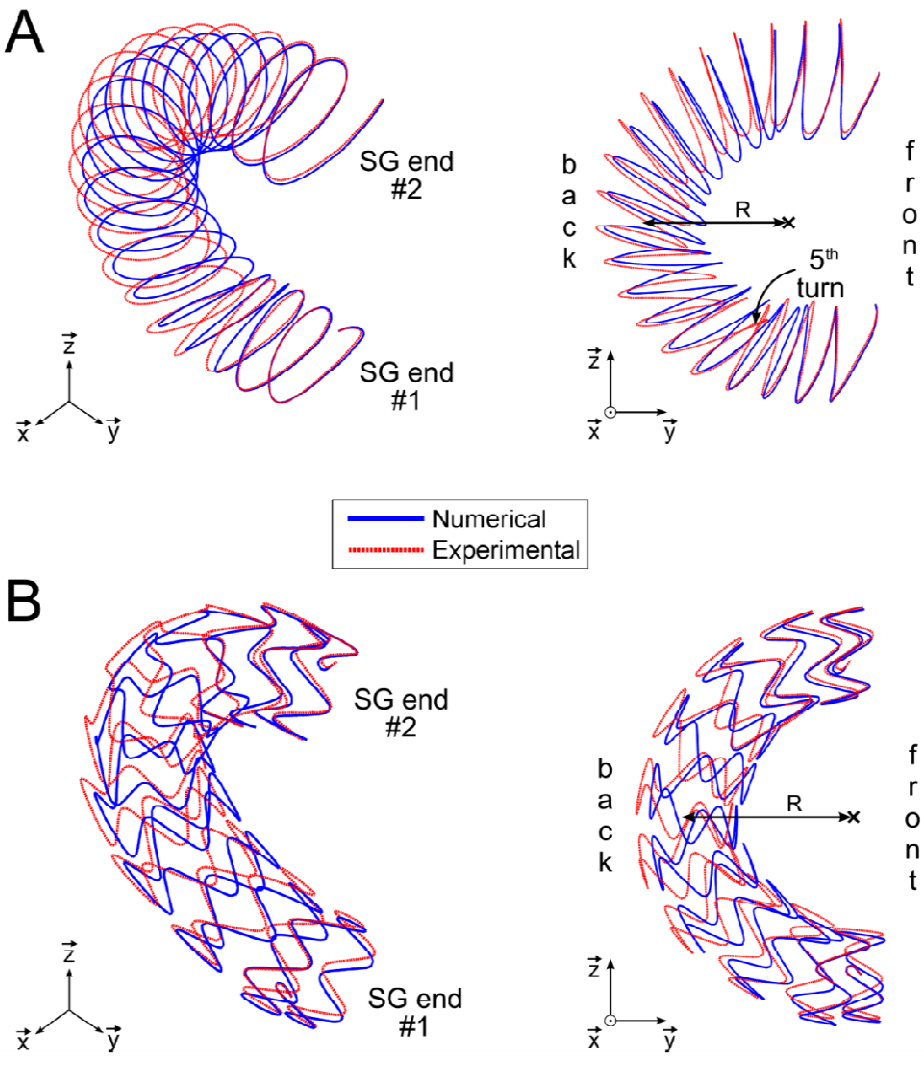

Figure 8 - 3D (left hand side) and 2D (right hand side) views of experimental and numerical deformed stents for Ao-SG (A) and Zs-SG (B).

b. Quantitative comparison

To better analyze the results, the evolution of position error δ along the curvilinear abscissa s of the bent stent centerlines was plotted for each SG in figure 9. The global radii of curvature R of the SGs were found to be equal to 20.5 mm and 24 mm for Ao-SG and Zs-SG, respectively (see figure 8). Results presented in this figure confirm the observations stated in the last subsection. Indeed, for Ao-SG (resp. Zs-SG), the position error oscillated between 0 and 20% (resp. 0 and 16%) with a mean value of 8.53% (resp. 6.41%) and the most important position error was approximately located at 570 mm (490 mm, respectively) from SG end #1.

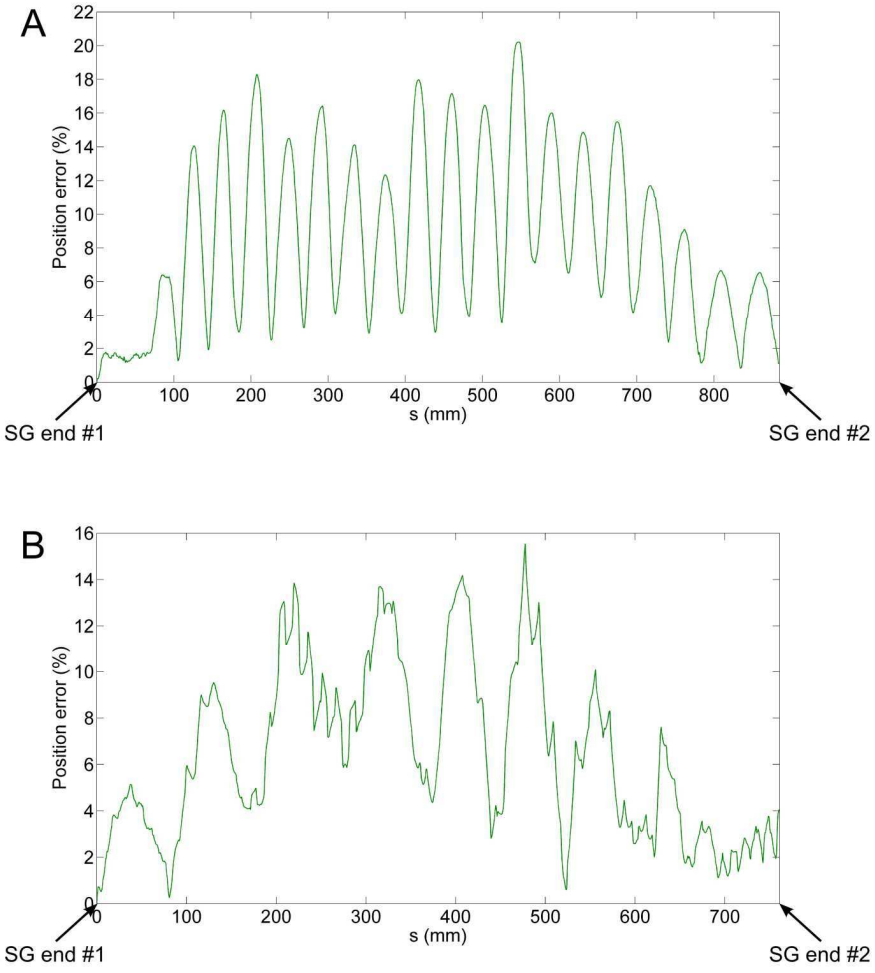

Figure 9 - Evolution of the position error δ along the stent centerline curvilinear abscissa *s* for Ao-SG (A) and Zs-SG (B).

All these results are supported by figure 10 that plots the evolution of experimental and numerical curvatures κ along the curvilinear abscissa *s* of the bent stent centerlines. For Ao-SG, the curvature of the numerical (resp. experimental) stent centerline generally oscillates between 0.06 and 0.22 mm^{-1} (resp. 0.03 and 0.22 mm^{-1}) with a mean of 0.143 mm^{-1} (resp. 0.144 mm^{-1}). For Zs-SG, the curvature of the numerical (resp. experimental) stent centerline oscillates between 0 and 1.17 mm^{-1} (resp. 0 and 1.17 mm^{-1}) with a mean of 0.278 mm^{-1} (resp. 0.275 mm^{-1}). For both SGs, the comparison between experimental data and simulated results is satisfactory, keeping in mind the systematic error $\Delta\kappa \approx \pm 0.01$ mm^{-1} induced during the estimation of the curvatures.

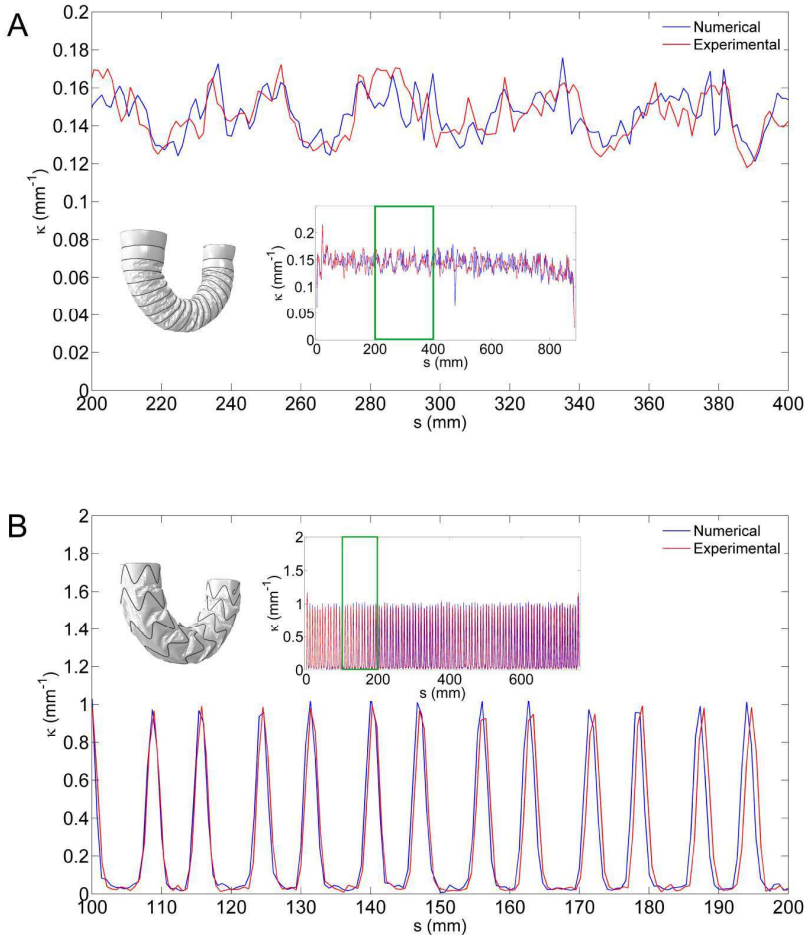

Figure 10 - Curvatures κ of both experimental and numerical deformed stent centerlines as functions of the stent centerline curvilinear abscissa s for Ao-SG (A) and Zs-SG (B).

To strengthen the above remarks, the experimental and numerical maximal bending strains ε_b^{max} recorded along the curvilinear abscissa s of the stents were finally estimated and compared (result not plotted here). For the two SGs, the experimental and numerical bending strains were found to be very close and very small, *i.e.* within the systematic error of 2.10^{-3}. This proves that during the studied bending of the SGs, no noticeable stent bending was observed. This also emphasizes the fairly good comparison between the experiments and the simulations.

Discussion

The objective of this study was to validate a numerical tool dedicated to predict the deformation of endovascular SGs, by comparing simulation results to what was observed from experiments. To run such a comparison, special attention was paid in order to minimize most of the possible error sources.

The mechanical behaviors of the stents and the grafts were modeled with appropriate constitutive laws, taking into account the possible superelastic behavior of NiTi and the strong anisotropy of polyester. In this last case, special mechanical tests were required and achieved prior to the simulation in order to gauge the stiffness and the anisotropy of the grafts.

The initial geometries of the experimental and numerical stents were set identical. This was possible thanks to the X-ray microtomography combined with dedicated image analysis subroutines.

The SGs were deformed with a special bending apparatus that was mounted within the microtomograph. This allowed (i) proper boundary conditions for the simulation to be captured directly from the experiments and (ii) the full final stent geometries to be determined to constitute an exhaustive experimental database for the comparison with the simulations.

By adopting this careful methodology, the very promising results that were obtained in this study bring the following comments.

The qualitative results displayed in figures 7 and 8 highlight an overall good agreement between experiments and numerical simulations of SGs' bending, except in some zones such as the fifth turn of the Ao stent: the observed difference is mainly due to the thick graft seam line, which was not modeled numerically. Indeed, Ao graft was composed of two pieces of graft sewn together along the entire length of the SG. It generated a high degree of

heterogeneity and caused the penetration of the fifth turn of the spiral stent within the Ao-SG during the bending.

Regarding the quantitative results, *i.e.* the position errors δ (see figure 9), the centerline curvatures κ (see figure 10) and the maximal bending strains ${\varepsilon_b}^{max}$, the agreement is still satisfactory. The mean (< 9 %) and maximal (< 20 %) position error between the simulated and imaged deformed stents remained fairly low for both SGs. Knowing that the mean position error for both SGs does not exceed 1.8 mm, the results of this work are acceptable if this value is compared to the observation scale commonly used in medical imaging. Furthermore, curvatures of experimentally and numerically bent stents were very close. Thus, maximal experimental and numerical bending strains were identical and negligible.

By using the results of the simulations, the corresponding maximal Von Mises strain was found to be equal to 0.37 % for Ao-SG and 0.36 % for Zs-SG. These very low strains entirely validate our initial basic choice concerning the stent constitutive behavior: during the considered SG bending, the whole stents remained elastic.

To the best of the authors' knowledge, very few studies were carried out on the experimental validation of numerical models of stents alone from a quantitative point of view [22, 31]. The experimental modalities used in these two studies on stent expansion are mainly based on 2D observations (measurements on pictures obtained with a CCD camera). Knowing that stent deployment and SG modeling are two distinct problems (consideration of the fabric which has a significant influence on SG behavior), it was necessary to develop a new methodology based on 3D data to validate quantitatively our SG numerical models. Besides, our study is the first in which such a methodology is carried out in the case of endovascular SGs. Considering the obtained results, and keeping in mind the complexity of the highly non-linear boundary values problems that were solved (large transformations, membrane

wrinkling, non-linear constitutive laws, self-contact problems), it is fair to consider that our SG numerical models are accurate and reliable enough to correctly reproduce the mechanical behavior of actual SG samples. Obviously, there are some differences between experimental and numerical results. However, these differences could be minimized by considering the following points in future simulations.

Most of the observed differences between the deformed imaged and numerical SGs probably come from the difficulty to model the initial shape of the grafts. Looking at the initial actual SG samples, one can clearly see that their fabrics form wrinkles (see figure 2) while the modeled SGs exhibit a rather smooth fabric surface without wrinkle (see figure 6). These initial real wrinkles constitute additional material available in the outer curvature region during the bending. Thus, they are suspected to induce a higher radius of curvature for the imaged SGs than for the numerical ones (see figure 8). A possible way to get rid of this would consist in improving the 3D imaging of the SGs, *e.g.* by enhancing the x-ray absorption of the grafts with contrast agents [12].

Differences also come from the elementary model used for the stent/graft connection. Indeed, the sutures between stent and graft were not modeled rigorously because this would have increased dramatically the complexity and the duration of calculations. This connection was considered perfect, although Ao sutures were coarse and allowed stent micro-movements.

The numerical boundary conditions were adjusted to the nearest experimental ones. However, in the case of the Zs-SG, some technical problems were encountered during the experiments and induced some slight differences between experimental and numerical boundary conditions. Indeed, the extremities of Zs-SG were not modeled while they were used for the embedding of the SG in the experiments, leading to a slight shear of the fabric in the non-embedded part of the Zs-SG (see figure 8).

Keeping in mind that the previous mentioned points should be tackled in future studies to improve the accuracy of the numerical SG models, this work has proven the relevance of the presented simulations from a mechanical viewpoint. To illustrate their usefulness, each bent SG was also subjected to an intraluminal pressure varying between the diastolic (75 mmHg) and systolic (150 mmHg) pressures (representative of a hypertensive patient). As an example, figure 11 shows the simulated deformed SGs with and without an intraluminal pressure of 150 mmHg. For both SGs, the visual comparison between pressurized and pressure-free geometries does not reveal any remarkable difference. For instance, by increasing the pressure, the fabric swells between stent turns, especially for Ao-SG whose fabric is softer and more flexible than the Zs-SG fabric (see table 2). Furthermore, the local curvature of the stent centerline was computed following the procedure adopted previously, showing a slight increase of this curvature (less than 10 % of the mean value) for both SGs. Likewise, the maximal stress value σ_S^{max} and the maximal variations of stresses max($\Delta\sigma_S$) in the stents for diastolic and systolic pressures were assessed and compared. First of all, for both SGs, σ_S^{max} values revealed that the stents remained elastic for this loading case (σ_S^{max} = 238 MPa for Ao-SG and σ_S^{max} = 241 MPa for Zs-SG). Thus, no marked martensitic transformation was observed within the stents. The intraluminal pressure variation is such that max($\Delta\sigma_S$) = 123 MPa for Ao-SG and max($\Delta\sigma_S$) = 70 MPa for Zs-SG. These values corresponded to a maximal variation of strain max($\Delta\varepsilon_S$) of 0.31 % for Ao-SG and 0.17 % for Zs-SG. Even if such tests and related results are still quite far from the clinical reality, these type of results could be useful for predicting stents' fatigue and durability [23, 27].

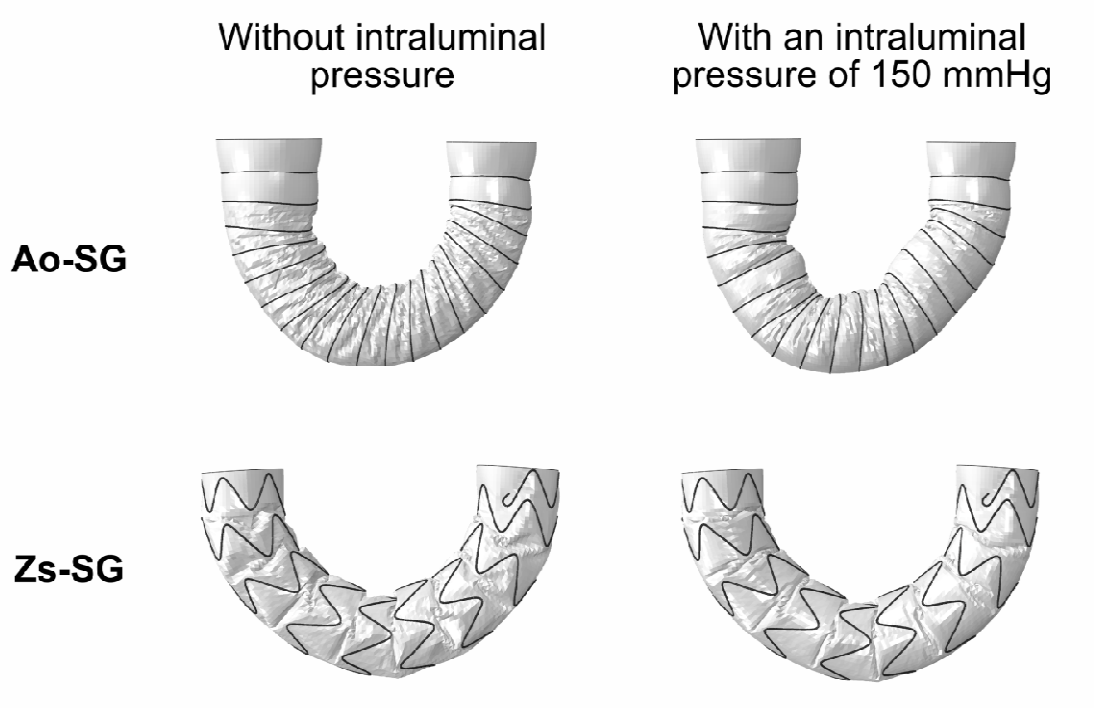

Figure 11 - Deformed Ao (upper pictures) and Zs-SGs (lower pictures) after simulations with (right hand side) or without (left hand side) intraluminal pressure (150 mmHg).

Conclusion

Thanks to proper bending experiments achieved inside a x-ray microtomograph, the numerical approach used to model aortic SGs and developed in Demanget *et al.* (2012) [13] could be validated. Indeed, skeletons of imaged and deformed stents were quantitatively compared to the numerical simulations, and a good agreement was found between experiments and simulations. This validation offers promising perspectives to implementing the numerical models in a computer-aided tool and simulating the endovascular treatments.

Acknowledgements

The authors gratefully acknowledge the Région Rhône-Alpes and the ANR (research program ‘‘3D discrete ANAlysis of micromechanisms of deformation in highly concentrated FIBre suspensions’’, ANAFIB, ANR-09-JCJC-0030-01) for their financial support.

References

[1]Albertini, J. N., J. A. Macierewicz, S. W. Yusuf, P. W. Wenham, and B. R. Hopkinson. Pathophysiology of proximal perigraft endoleak following endovascular repair of abdominal aortic aneurysms: a study using a flow model. Eur. J. Vasc. Endovasc. Surg. 22:53-56, 2001.

[2]Albertini, J. N., T. Perdikides, C. V. Soong, R. J. Hinchliffe, M. Trojanowksa, S. W. Yusuf, C. Clement, and B. R. Hopkinson. Endovascular repair of abdominal aortic aneurysms in patients with severe angulation of the proximal neck using a flexible stent-graft: European Multicenter Experience. J. Cardiovasc. Surg. 47:245-250, 2006.

[3]Auricchio, F., M. Conti, M. De Beule, G. De Santis, and B. Verhegghe. Carotid artery stenting simulation: From patient-specific images to finite element analysis. Med. Eng. Phys. 33:281-289, 2011.

[4]Badel, P., E. Vidal-Salle, E. Maire, and P. Boisse. Simulation and tomography analysis of textile composite reinforcement deformation at the mesoscopic scale. Compos. Sci. Technol. 68:2433-2440, 2008.

[5]Baum, R. A., S. W. Stavropoulos, R. M. Fairman, and J. P. Carpenter. Endoleaks after endovascular repair of abdominal aortic aneurysms. J. Vasc. Interv. Radiol. 14:1111-1117, 2003.

[6]Beebe, H. G., J. L. Cronenwett, B. T. Katzen, D. C. Brewster, and R. M. Green. Results of an aortic endograft trial: Impact of device failure beyond 12 months. J. Vasc. Surg. 33:S55-S63, 2001.

[7]Buffiere, J. Y., E. Maire, J. Adrien, J. P. Masse, and E. Boller. In Situ Experiments with X ray Tomography: an Attractive Tool for Experimental Mechanics. Exp. Mech. 50:289-305, 2010.

[8]Carroccio, A., P. L. Faries, N. J. Morrissey, V. Teodorescu, J. A. Burks, E. C. Gravereaux, L. H. Hollier, and M. L. Marin. Predicting iliac limb occlusions after bifurcated aortic stent grafting: Anatomic and device-related causes. J. Vasc. Surg. 36:679-684, 2002.

[9]Chakfe, N., F. Dieval, G. Riepe, D. Mathieu, I. Zbali, F. Thaveau, C. Heintz, J. G. Kretz, and B. Durand. Influence of the textile structure on the degradation of explanted aortic endoprostheses. Eur. J. Vasc. Endovasc. Surg. 27:33-41, 2004.

[10]Cochennec, F., J. P. Becquemin, P. Desgranges, E. Allaire, H. Kobeiter, and F. Roudot-Thoraval. Limb graft occlusion following EVAR: Clinical pattern, outcomes and predictive factors of occurrence. Eur. J. Vasc. Endovasc. Surg. 34:59-65, 2007.

[11]Connolley, T., D. Nash, J. Y. Buffiere, F. Sharif, P. E. McHugh. X-ray micro-tomography of a coronary stent deployed in a model artery. Med. Eng. Phys. 29:1132-1141, 2007.

[12]Davit, Y., G. Iltis, G. Debenest, S. Veran-Tissoires, D. Wildenschild, M. Gerino, and M. Quintard. Imaging biofilm in porous media using X-ray computed microtomography. J. Microsc. 242:15-25, 2011.

[13]Demanget, N., S. Avril, P. Badel, L. Orgéas, C. Geindreau, J. N. Albertini, and J. P. Favre. Computational comparison of the bending behavior of aortic stent-grafts. J. Mech. Behav. Biomed. Mater. 5:272-282, 2012.

[14]Elliott, J. A., A. H. Windle, J. R. Hobdell, G. Eeckhaut, R. J. Oldman, W. Ludwig, E. Boller, P. Cloetens, and J. Baruchel. In-situ deformation of an open-cell flexible polyurethane foam characterised by 3D computed microtomography. J. Mater. Sci. 37:1547-1555, 2002.

[15]Favier D., L. Orgéas, D. Ferrier, P. Poncin, and Y. Liu. Influence of manufacturing methods on the homogeneity and properties of Nitinol tubular stents. J. Phys. IV. 11:541-546, 2001.

[16]Hall G. J., and E. P. Kasper. Comparison of element technologies for modeling stent expansion. J. Biomech. Eng. - T. ASME 128:751-756, 2006.

[17]Jacobs, T. S., J. Won, E. C. Gravereaux, P. L. Faries, N. Morrissey, V. J. Teodorescu, L. H. Hollier, and M. L. Marin. Mechanical failure of prosthetic human implants: A 10-year experience with aortic stent graft devices. J. Vasc. Surg. 37:16-26, 2003.

[18]Klein, A., J. A. van der Vliet, L. J. Oostveen, Y. Hoogeveen, J. J. S. Kool, W. K. J. Renema, and C. H. Slump. Automatic segmentation of the wire frame of stent grafts from CT data. Med. Image Anal. 16:127-139, 2012.

[19]Kleinstreuer, C., Z. Li, C. A. Basciano, S. Seelecke, and M. A. Farber. Computational mechanics of Nitinol stent grafts. J. Biomech. 41:2370-2378, 2008.

[20]Latil, P., L. Orgéas, C. Geindreau, P. J. J. Dumont, and S. Rollant du Roscoat. Towards the 3D *in situ* characterisation of deformation micro-mechanisms within a compressed bundle of fibres. Compos. Sci. Technol. 71:480-488, 2011.

[21]Le, T. H., P. J. J. Dumont, L. Orgeas, D. Favier, L. Salvo, and E. Boller. X-ray phase contrast microtomography for the analysis of the fibrous microstructure of SMC composites. Compos. Part. A. 39:91-103, 2008.

[22]Migliavacca, F., L. Petrini, V. Montanari, I. Quagliana, F. Auricchio, and G. Dubini. A predictive study of the mechanical behavior of coronary stents by computer modelling. Med. Eng. Phys. 27:13-18, 2005.

[23]Miyazaki, S. K. Mizukoshi, T. Ueki, T. Sakuma, and Y. N. Liu. Fatigue life of Ti-50 at.% Ni and Ti-40Ni-10Cu (at.%) shape memory alloy wires. Mat. Sci. Eng. A-struct. 273:658-663, 1999.

[24]Mortier, P., M. De Beule, D. Van Loo, B. Masschaele, P. Verdonck, and B. Verhegghe. Automated generation of a finite element stent model. Med. Biol. Eng. Comput. 46:1169-1173, 2008.

[25]Orgéas, L., and D. Favier. Non-symmetric tension-compression behavior of NiTi alloy. J. Phys. IV C8:593-598, 1995.

[26]Orgéas, L., and D. Favier. Stress-induced martensitic transformation of a NiTi alloy in isothermal shear, tension and compression. Acta Mater. 46:5579-5591, 1998.

[27]Pelton, A. R., J. DiCello, and S. Miyazaki. Optimisation of processing and properties of medical grade Nitinol wire. Min. Invas. Ther. & Allied Technol. 9:107-118, 2000.

[28]Pelton, A. R., V. Schroeder, M. R. Mitchell, X. Y. Gong, M. Barney, and S. W. Robertson. Fatigue and durability of Nitinol stents. J. Mech. Behav. Biomed. Mater. 1:153-164, 2008.

[29]Stock, S. R. X-ray microtomography of materials. Int. Mater. Rev. 44:141-164, 1999.

[30]Stock, S. R. Recent advances in X-ray microtomography applied to materials. Int. Mater. Rev. 53:129-181, 2008.

[31]Takashima, K., T. Kitou, K. Mori, and K. Ikeuchi. Simulation and experimental observation of contact conditions between stents and artery models. Med. Eng. Phys. 29:326-335, 2007.

[32]Vad, S., A. Eskinazi, T. Corbett, T. McGloughlin, and J. P. Vande Geest. Determination of Coefficient of Friction for Self-Expanding Stent-Grafts. J. Biomech. Eng. - T. ASME 132:121007, 2010.